Nonlinear Photoluminescence Spectrum of Single Gold Nanostructures

Vanessa Knittel,[†] Marco P. Fischer,[†] Tjaard de Roo,[‡] Stefan Mecking,[‡] Alfred Leitenstorfer,[†] and Daniele Brida*[,†]

[†]Department of Physics and Center for Applied Photonics, University of Konstanz, D-78457 Konstanz, Germany and [‡]Department of Chemistry and Center for Applied Photonics, University of Konstanz, D-78457 Konstanz, Germany

ABSTRACT We investigate the multiphoton photoluminescence characteristics of gold nanoantennas fabricated from single crystals and polycrystalline films. By exciting these nanostructures with ultrashort pulses tunable in the near-infrared range, we observe distinct features in the broadband photoluminescence spectrum. By comparing antennas of different crystallinity and shape, we demonstrate that the nanoscopic geometry of plasmonic devices determines the shape of the emission spectra. Our findings rule out the contribution of the gold band structure in shaping the photoluminescence.

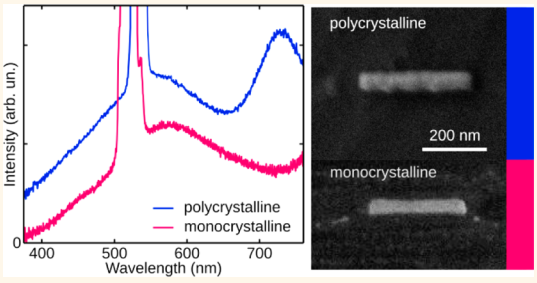

KEYWORDS: nanoplasmonics · nanoantennas · nonlinear optics · photoluminescence · multiphoton processes · third-harmonic generation

In recent years, metal nanoantennas have revolutionized the investigation of light-matter-interaction[1,2] thanks to the ability to confine optical fields to volumes much smaller than the diffraction limit.[3−5] The outstanding field enhancement that they provide is exploited, for example, to boost the performances of single photon nano-emitters such as quantum dots[6,7] and to increase the sensing capabilities of weak signals at the nanoscale.[8,9] Nanoantennas are also ideally suited as local emitters by driving nonlinear processes in the near-field such as third-harmonic generation (THG)[10] as well as processes of even higher orders.[11,12] In addition, nonlinear frequency mixing in nanostructures is always paralleled by the incoherent generation of multiphoton photoluminescence (MPPL) in the visible and near-infrared. This process is widely exploited in two-photon photoluminescence imaging.[13−15]

A full understanding of MPPL mechanisms is crucial for a number of applications. In particular, the emission of photoluminescence (PL) overlaps with the coherent optical response of the nanoantenna system and of quantum objects positioned in the field enhancement region. Thus, precise control of the PL is required, especially in nanostructures where this process is significantly enhanced.[16−18]

As sketched in Figure 1a, MPPL in gold is triggered by sequential steps of photon absorption:[19,20] one or more intraband transitions within the sp-conduction band are followed by an interband excitation that leads to the creation of a d-band hole. PL is then generated by the radiative recombination of electrons in the conduction band with the holes in d-band. The typical PL spectrum as generated by gold nanostructures extends from the visible range to the near-infrared and presents distinct broad peaks at different spectral positions.[2,17,21] The fundamental reasons for this finding were not well understood up to now. Early explanations ascribe the PL spectral features to increased density of states for electron−hole recombination near the X and L symmetry points in the gold band structure.[17,21−23]

In this work, we investigate the key features of gold PL to determine their origin. We find that the band structure plays a minor role in the characteristics of the spectral emission. Instead, we show that the PL features arise from the specific antenna geometry and its linear optical response despite the nonlinear mechanisms at the core of the multiphoton PL process. For this reason, nanoantennas are also strongly affected by the crystallinity degree of gold.

* Address correspondence to daniele.brida@uni-konstanz.de.

Received for review November 20, 2014 and accepted December 30, 2014.

Published online December 30, 2014
10.1021/nn5066233

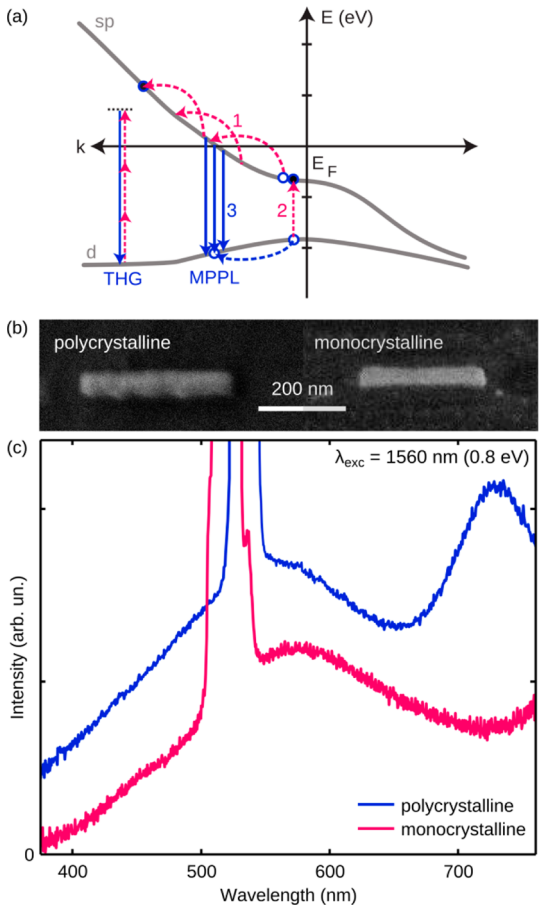

Figure 1. (a) Sketch of the MPPL and THG process within the gold band structure (gray) near the L symmetry point. MPPL generation consists of a cascade of intraband absorptions (1) that enables an interband transition (2) resulting in a hole in the d-band. PL is the result of radiative recombination of sp-electrons with the hole (3). The coherent THG process is not necessarily resonant with optical transitions. (b) SEM images of a poly- and a monocrystalline nanorod with dimensions of 370 nm × 60 nm and 310 nm × 60 nm, respectively. (c) Typical photoluminescence spectra obtained from the polycrystalline (blue curve) and monocrystalline (red curve) nanorod depicted in the upper panel. The optical excitation is set to a wavelength of 1560 nm (0.79 eV). A 110 pJ pulse energy was measured before coupling into the microscope. The distinct third-harmonic peak is cropped to highlight the spectral structure of the broadband PL.

In our experiments, we detect polarization-resolved MPPL in single- and polycrystalline nanoantennas triggered by ultrashort laser pulses in the near-infrared and combine the experimental results with boundary element simulations. The comparison between different crystallinities of the antenna specimens allows us to conclusively rule out the contribution of specific gold band structure features in shaping the nonlinear PL emission.

RESULTS AND DISCUSSION

For the measurements, we use custom-tailored poly- and monocrystalline gold nanoantennas on a polished fused silica substrate (see Figure 1b). The polycrystalline nanostructures are fabricated with electron beam lithography. Instead, single-crystal antennas are milled with focused ion beam (FIB)[24] into flat monocrystalline gold synthesized in a wet-chemical process.[25,26] This approach allows us to fully control the size of the gold nanoantenna, its resonance and orientation with respect to the crystallographic axes, thereby enabling easy identification of different contributions to the PL spectral behavior.

For simplicity and to minimize the influence of the antenna shape, we investigate mainly single nanorods. Their width is kept at a value around 50 nm and their length is varied from 170 to 480 nm to tune their plasmonic resonance from a wavelength of 1100–2100 nm. The thickness of both sample types is approximately 30 nm.

The gold nanoantennas are excited optically by using a femtosecond Er:fiber laser system, producing pulses widely tunable from a wavelength of 1000–2100 nm thanks to a tailor-cut highly nonlinear fiber[27,28] (see Supporting Information, Figure 1). In the experiments, the average excitation power is adjusted between 2 and 7 mW at 40 MHz repetition rate, corresponding to pulse energies between 50 and 175 pJ, and the pulse bandwidth is limited to 8 THz. The infrared excitation allows us to observe highly nonlinear effects, such as MPPL and THG emitted in the visible range. The large wavelength difference between excitation and emission allows for easy spectral separation.

Using all-reflective optics, we focus the tunable pulses on single antennas with polarization set parallel to the long antenna axis. The nonlinear antenna emission is spectrally dispersed and detected by a CCD array. The nonlinear emission from the nanoantennas is integrated over a time interval of 180 s.

Figure 1c displays the typical PL emission obtained from polycrystalline (blue curve) and monocrystalline (red curve) nanorods. The spectra are dominated by a narrow THG peak superimposed to the broad PL emission. Independent of the crystallinity, we observe a PL peak in the green spectral range at a position of approximately 570 nm as well as enhanced emission in the red wing. Interestingly, only polycrystalline antennas feature a distinct second PL maximum at a wavelength of 730 nm. The excitation wavelength was set to 1560 nm. However, the spectral characteristics of the PL in mono- and polycrystalline antennas are essentially reproduced for all excitation wavelengths ranging from 1300 to 2030 nm, except for the obvious shifting of the THG peak. The green PL peak only slightly varies its spectral position from one antenna to the other, whereas the red maximum that appears only in polycrystalline samples red-shifts from 710 to 790 nm with increasing antenna length (see Supporting Information, Figure 2). The relative intensity of the peaks depends on the individual antenna and to some extent on the excitation power. The PL spectral structure

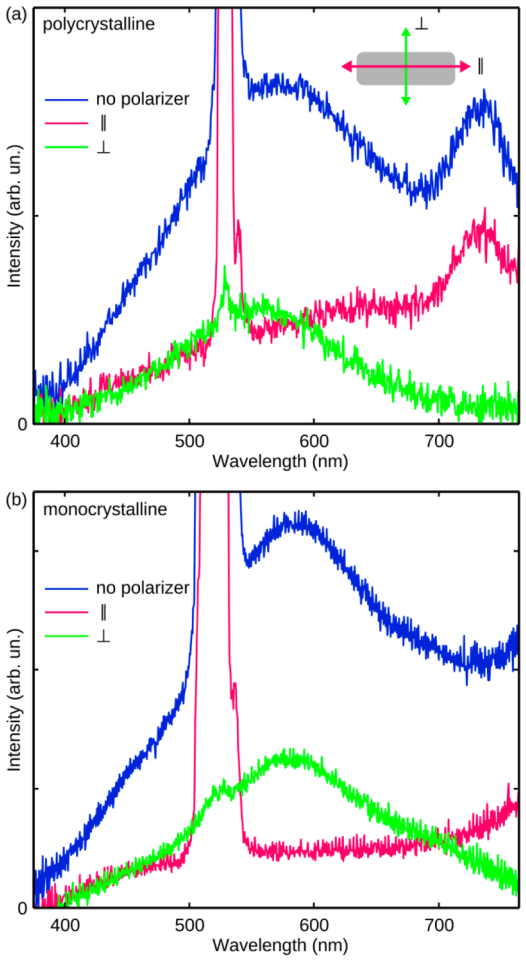

Figure 2. Polarization-resolved photoluminescence spectra from a polycrystalline (a) and a monocrystalline (b) nanorod. Antenna emission was collected without polarizer (blue curves) and with polarizer set parallel (red curves) or perpendicular (green curves) to the long rod axis as indicated in the inset sketch in panel a. Excitation wavelength was set to 1560 nm (0.79 eV).

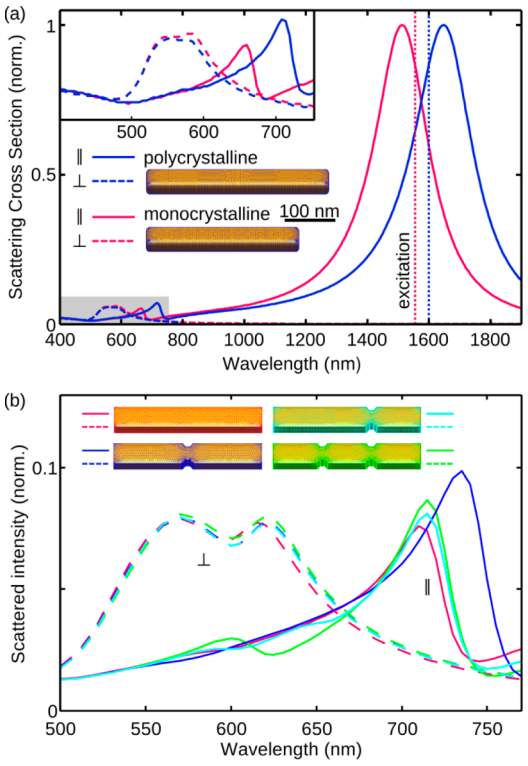

Figure 3. Boundary element simulations of the scattering spectra of the nanoantennas featured in Figure 1. (a) Results from a polycrystalline (blue curves) and a monocrystalline rod (red curves), for light polarization set parallel (solid line) or perpendicular to the long antenna axis (dashed line), respectively. The dotted lines indicate the center wavelength of the experimental excitation pulse. The graph in the inset shows a magnification of the shaded area. (b) Full lines: effect of symmetric and asymmetric defects of the antenna structure on the second-order resonance (blue, green and turquoise) that appears always enhanced as compared to the single-crystal case (red). In contrast, the perpendicular resonance (dashed) is hardly influenced by the degree of crystallinity.

is not influenced by the nonlinear order of the process exploited for the creation of a hole in the d-band. In fact, excitation at 1560 nm leads to a 4-photon PL whereas at longer wavelengths the process involves 5 photons (see Supporting Information, Figure 2).

The difference in the spectral shape between monocrystalline and polycrystalline samples already indicates that the bulk electronic band structure is not solely responsible for the PL profile. Analysis of the polarization behavior of the PL emission reveals further details to determine the origin of the peaks.

Figure 2 shows PL spectra from a polycrystalline (a) and a monocrystalline (b) rod acquired by selecting the light polarization by means of a polarizer placed in front of the detection unit. The polarizer is set either parallel or perpendicular (red and green curve, respectively) to the long rod axis (see sketch in Figure 2a). For comparison, the corresponding spectra taken without polarizer are depicted in blue. The PL structure can be decomposed into a peak centered around 600 nm that is polarized along the perpendicular direction, and a PL component above 700 nm with polarization parallel to the rod. Both crystallinity configurations exhibit a broad underlying plateau polarized in parallel direction. It should be noted, however, that this broad PL feature is more structured in polycrystalline antennas and shows significant variability with respect to the specimen investigated in the experiments.

The polarization behavior allows us to ascribe the origin of the peaks to specific plasmonic resonances of the nanoantenna. This fact is illustrated in Figure 3a with numerical simulations based on a boundary element method (BEM).[29,30] The scattering cross sections for a polycrystalline (blue curves) and a monocrystalline structure (red curves) with dimensions analog to the antennas employed for the experimental data is shown in Figure 1.

The scattering cross section for polarization parallel to the long axis of the rod verifies that the plasmonic resonance in the near-infrared matches the excitation wavelength. In the red part of the visible spectrum (see also inset in Figure 3a), we obtain a second-order resonance at a wavelength of 710 nm for the

polycrystalline antenna. Remarkably, the shorter monocrystalline antenna features only a smaller and blue-shifted second-order resonance. Obviously, the simulations are not able to grasp why the monocrystalline antenna is experimentally shorter than the polycrystalline one while keeping the same frequency for the fundamental resonance. We argue that the density of gold in polycrystalline specimens is lower due to the nanoscopic grainy structure of the nanoantennas resulting in a slightly different dielectric response. Both antennas, however, exhibit a broad perpendicular resonance in the green visible range at a wavelength of approximately 575 nm.

The transverse resonance enhances green PL emission polarized perpendicular to the antenna axis. Since this resonance is very broad and mainly determined by the antenna width, we observe small variation in the peak position depending on the specimen, as mentioned earlier. This finding results from slight variation of the rod width in the range of 40−60 nm. Analog to the transverse case, the second-order resonance enhances the red emission in parallel direction, resulting in a distinct peak for polycrystalline antennas. This fact is explained with the more complex structure in polycrystalline nanoparticles. In particular, the considerable length difference between mono- and polycrystalline rods when resonant at the same wavelength seems to play a crucial role. The longer the antenna is, in fact, the stronger the second order resonance becomes, thus affecting the intensity of the corresponding PL emitted. We also argue that the grain boundaries and the overall geometrical structure in polycrystalline antennas affect the resonances, thereby further enhancing the second-order response. Figure 3b shows simulations of a plasmonic antenna with some indentations to mimic the defective internal structure that can be observed in polycrystalline samples. Any artificial perturbation has the only effect of enhancing the second order-peak independent of the symmetry of the defects with respect to the antenna general shape. The grainy structure combined with an overall longer dimension makes polycrystalline antennas prone to show a strong red PL peak in addition to the green one.

Similar polarization behavior of the PL was previously observed[21] but assigned to different orientations within the monocrystalline nanorods with respect to the crystallographic axes of gold. To rule out this argument, we accurately fabricated antennas with different crystal orientations and found no detectable influence as can be seen in Figure 4.

Typical nonlinear spectra are shown for two differently orientated antennas as indicated in the inset. There is no noticeable dependence on the orientation toward the crystallographic axis. The same finding applies to the polarization behavior. The green PL peak (broadband feature centered at 600 nm) is slightly red-shifted with respect to the other samples presented in this work due to a different index of refraction of the

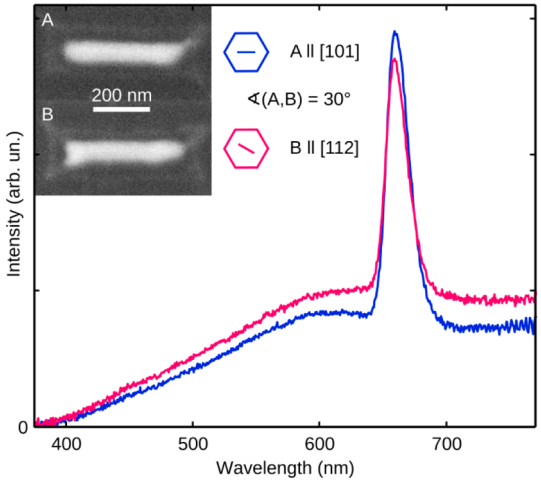

Figure 4. PL spectra obtained from two monocrystalline rod antennas with different orientation to the crystallographic axes: antenna A was aligned parallel to an edge of the hexagonal single crystal (blue curve), antenna B was rotated by 30° with respect to A (red curve). The excitation wavelength was set to 1980 nm (0.63 eV) at pulse energy of 88 pJ. In this case, a quartz substrate was used and the integration time was set to 300 s.

substrate which was crystalline quartz in this case. The sharp emission maximum at a wavelength of 660 nm is due to coherent third-harmonic generation.

Hence the polarization analysis points out that the spectral shape of the photoluminescence is dominated by the internal morphology and external geometry of the nanoantenna. The influence of the electronic band structure of gold is insignificant. It might contribute to a minor extent by providing a varying electronic joint density of states for the radiative recombination process that leads to PL. The influence of the external shape becomes even more evident when we move to a completely different geometry: Figure 5a compares the typical PL spectra of a monocrystalline bowtie antenna (blue curve) to that of a rod (red curve), both resonant at a wavelength of approximately 1560 nm.

Bowtie antennas exhibit a completely different PL spectrum that does not show the peaked structure typical of rod antennas. Instead, the emission is strongly unbalanced toward longer wavelengths. The corresponding BEM simulations of the scattering cross section reported in Figure 5b support the experimental findings. Essentially, the transverse resonance is less defined and red-shifted due to the fact that bowties are wider and tapered.

The differences between mono- and polycrystalline antennas confirm that, apart from the external geometry, the internal grain structure has strong influence. Interestingly, the crystalline grains themselves contribute to the PL spectral features as demonstrated in Figure 6a by means of two PL spectra obtained from two distinct polycrystalline rods under perfectly identical experimental conditions.

Only a small difference related to the respective internal grain structure (see SEM image in Figure 6a)

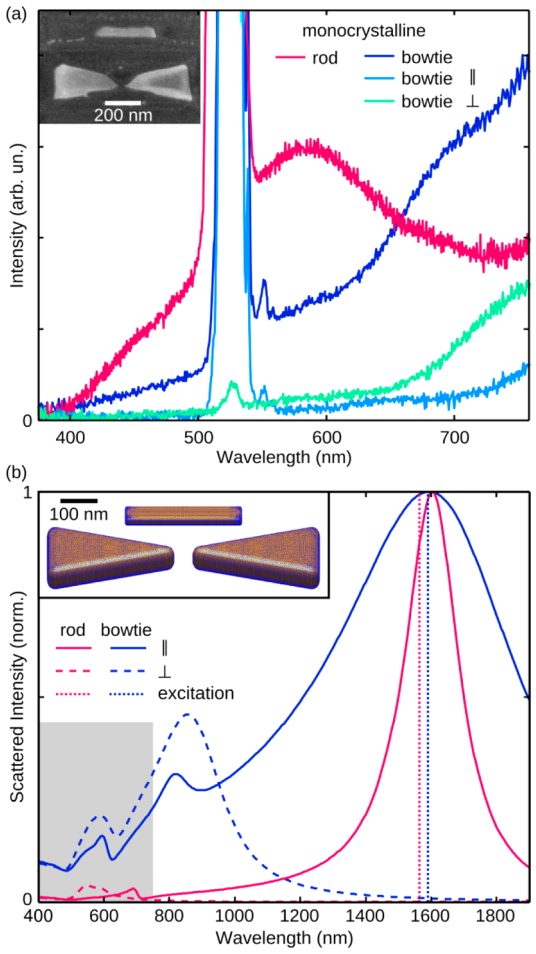

Figure 5. (a) PL spectra of a monocrystalline rod (red curve) and a bowtie antenna (blue curve) under excitation at a wavelength of 1560 nm (0.79 eV). SEM micrographs are shown in the inset. The light blue and green curves represent the bowtie PL spectra with polarization analyzer set parallel and perpendicular to the long antenna axis, respectively. (b) Boundary element simulations of the scattering spectra of nanoantennas with dimensions as in (a): rod (red curve) and bowtie (blue curve), for polarization set parallel (solid line) and perpendicular (dashed line) to the long antenna axis, respectively. The dotted vertical lines indicate the center wavelength of the experimental excitation pulses and the shaded area highlights the spectral range of the experimental data in (a).

discriminates between them. Without taking into account the nanoscopical geometry, the rods should have the same resonance behavior. However, the experimental data highlight that the individual grain influence leads to a major effect on the red PL peak as already pointed out by the simulations in Figure 3b. In particular, we can observe a spectral shift and a significant difference in the ratio between red and green PL peaks. A possible explanation relies on how

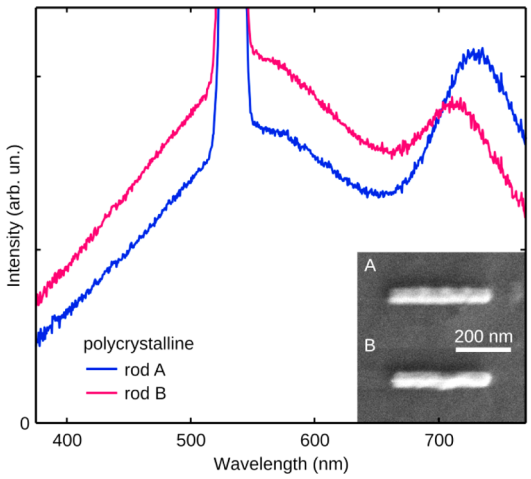

Figure 6. PL spectra obtained from two polycrystalline rods with different internal grain structure (observable in the inset SEM images) under otherwise identical experimental conditions. Excitation was set to a wavelength of 1590 nm (0.78 eV) with incident pulse energy of 110 pJ.

the complex internal substructure specific for each nanoantenna (due to the gold grains) perturbs the second-order plasmonic response.

CONCLUSIONS

Our investigation unveils the fundamental importance of the structural properties of gold plasmonic nanoantennas for the generation of PL and its spectral shape. Surprisingly, the linear properties of the antennas largely determine the spectral efficiency of the nonlinear emission. The radiative recombination process is only marginally affected by the joint density of states between the *sp* conduction band and the *d* band where the hole is nonlinearly created. This fact constitutes an important step in understanding how to control nonlinear emission at the nanoscale by optimizing geometry. In particular, the discovery of pronounced effects due to the internal morphology of single optical antennas motivates fabrication of devices with better reproducibility based on single-crystal material. Polycrystalline structures, in fact, prove to be prone to variability in the nonlinear optical response dictated by the random arrangement of the internal grain structure. The findings of this work are crucial for applications where plasmonic nanoantennas are coupled to quantum emitters and exploited for the enhancement of light-matter-interaction. MPPL, in fact, is a process that may be often considered as parasitic and detrimental, but it might even be successfully exploited for applications requiring a broadband and incoherent local excitation source.

METHODS

Nanoantenna Fabrication. We fabricate custom-tailored poly- and monocrystalline gold nanoantennas on a polished fused silica substrate (thickness 150 μm) with a 2 nm-thick Chromium adhesion layer. The polycrystalline nanostructures are fabricated with electron beam lithography, subsequent thermal

evaporation of gold and lift-off. Single-crystal antennas are milled with focused ion beam (FIB) into flat monocrystalline gold flakes (150 × 150 μm area and as thin as 50 nm) synthesized in a wet-chemical process.[25,26] In detail, a precursor (AuCl4)- is phase transferred from aqueous medium and stabilized in toluene by tetraoctylammonium bromide. The flakes can be further tinned during the FIB fabrication. The nanostructures are fully characterized by means of scanning electron microscopy (SEM) and atomic force microscopy.

Microscopy and Nonlinear Excitation. The femtosecond Er:fiber laser system used for optical excitation of the nanoantennas is home-built. The 150 fs pulses drive the generation of widely tunable spectral components from a wavelength of 1000 to 2100 nm by means of a tailor-cut highly nonlinear fiber[27,28] (see Supporting Information, Figure 1). The laser operates at 40 MHz repetition rate.

The microscope is based on all-reflective optics (Cassegrain objective, NA 0.65). The nonlinear antenna emission is collected by a high numerical-aperture dark field objective (NA 0.95) in transmission geometry, spectrally dispersed (grating monochromator Acton Spectra Pro 2300i) and detected by a CCD array (Andor Newton DU 920P-BU, Peltier-cooled to −70 °C). PL and THG are cleaned from residual of the fundamental excitation by a short pass filter (cutoff wavelength of 842 nm).

Numerical Simulations. The simulations solve Maxwell's equations based on a boundary element method (BEM).[29,30] For this purpose, the particle surface is discretized into triangles and quadrilaterals, their face centers serving as collocation points where the electromagnetic fields are calculated. The dielectric function of gold is based on experimental data;[31] the dielectric function of the embedding medium is calculated as weighted average[5] between the dielectric functions of fused silica[32] and air. Plane waves interacting with the nanostructure are applied with polarization set either parallel (solid lines) or perpendicular (dashed lines) to the long rod axis.

Conflict of Interest: The authors declare no competing financial interest.

Acknowledgment. This work was funded by the DFG *via* SFB767. D.B. acknowledges support by the Zukunftskolleg of University of Konstanz, the Eliteprogramm of Baden-Württemberg Stiftung and the Marie Curie CIG project "UltraQuEsT" no. 334463.

Supporting Information Available: Additional figures and experimental details. This material is available free of charge *via* the Internet at http://pubs.acs.org.

REFERENCES AND NOTES

1. Bharadwaj, P.; Deutsch, B.; Novotny, L. Optical Antennas. *Adv. Opt. Photonics* **2009**, *1*, 438–483.
2. Mühlschlegel, P.; Eisler, H.-J.; Martin, O. J. F.; Hecht, B.; Pohl, D. W. Resonant Optical Antennas. *Science* **2005**, *308*, 1607–1609.
3. Schuck, P. J.; Fromm, D. P.; Sundaramurthy, A.; Kino, G. S.; Moerner, W. E. Improving the Mismatch between Light and Nanoscale Objects with Gold Bowtie Nanoantennas. *Phys. Rev. Lett.* **2005**, *94*, 017402.
4. Ozbay, E. Plasmonics: Merging Photonics and Electronics at Nanoscale Dimensions. *Science* **2006**, *311*, 189–193.
5. Hanke, T.; Cesar, J.; Knittel, V.; Trügler, A.; Hohenester, U.; Leitenstorfer, A.; Bratschitsch, R. Tailoring Spatiotemporal Light Confinement in Single Plasmonic Nanoantennas. *Nano Lett.* **2012**, *12*, 992–996.
6. Curto, A. G.; Volpe, G.; Taminiau, T. H.; Kreuzer, M. P.; Quidant, R.; van Hulst, N. F. Unidirectional Emission of a Quantum Dot Coupled to a Nanoantenna. *Science* **2010**, *329*, 930–933.
7. Pfeiffer, M.; Lindfors, K.; Wolpert, C.; Atkinson, P.; Benyoucef, M.; Rastelli, A.; Schmidt, O. G.; Giessen, H.; Lippitz, M. Enhancing the Optical Excitation Efficiency of a Single Self-Assembled Quantum Dot with a Plasmonic Nanoantenna. *Nano Lett.* **2010**, *10*, 4555–4558.
8. Liu, N.; Tang, M. L.; Hentschel, M.; Giessen, H.; Alivisatos, A. P. Nanoantenna-enhanced Gas Sensing in a Single Tailored Nanofocus. *Nat. Mater.* **2011**, *10*, 631–636.
9. Lohmüller, T.; Iversen, L.; Schmidt, M.; Rhodes, C.; Tu, H.-L.; Lin, W.-C.; Groves, J. T. Single Molecule Tracking on Supported Membranes with Arrays of Optical Nanoantennas. *Nano Lett.* **2012**, *12*, 1717–1721.
10. Hanke, T.; Krauss, G.; Träutlein, D.; Wild, B.; Bratschitsch, R.; Leitenstorfer, A. Efficient Nonlinear Light Emission of Single Gold Optical Antennas Driven by Few-Cycle Near-Infrared Pulses. *Phys. Rev. Lett.* **2009**, *103*, 257404.
11. Pfullmann, N.; Waltermann, C.; Kovačev, M.; Knittel, V.; Bratschitsch, R.; Akemeier, D.; Hütten, A.; Leitenstorfer, A.; Morgner, U. Nanoantenna-Assisted Harmonic Generation. *Appl. Phys. B: Lasers Opt.* **2013**, *113*, 75–79.
12. Danckwerts, M.; Novotny, L. Optical Frequency Mixing at Coupled Gold Nanoparticles. *Phys. Rev. Lett.* **2007**, *98*, 026104.
13. Ghenuche, P.; Cherukulappurath, S.; Taminiau, T. H.; van Hulst, N. F.; Quidant, R. Spectroscopic Mode Mapping of Resonant Plasmon Nanoantennas. *Phys. Rev. Lett.* **2008**, *101*, 116805.
14. Huang, J.-S.; Kern, J.; Geisler, P.; Weinmann, P.; Kamp, M.; Forchel, A.; Biagioni, P.; Hecht, B. Mode Imaging and Selection in Strongly Coupled Nanoantennas. *Nano Lett.* **2010**, *10*, 2105–2110.
15. Durr, N. J.; Larson, T.; Smith, D. K.; Korgel, B. A.; Sokolov, K.; Ben-Yakar, A. Two-photon Luminescence Imaging of Cancer Cells Using Molecularly Targeted Gold Nanorods. *Nano Lett.* **2007**, *7*, 941–945.
16. Farrer, R. A.; Butterfield, F. L.; Chen, V. W.; Fourkas, J. T. Highly Efficient Multiphoton-Absorption-Induced Luminescence from Gold Nanoparticles. *Nano Lett.* **2005**, *5*, 1139–1142.
17. Beversluis, M. R.; Bouhelier, A.; Novotny, L. Continuum Generation from Single Gold Nanostructures through Near-Field Mediated Intraband Transitions. *Phys. Rev. B* **2003**, *68*, 115433.
18. Ropers, C.; Solli, D. R.; Schulz, C. P.; Lienau, C.; Elsaesser, T. Localized Multiphoton Emission of Femtosecond Electron Pulses from Metal Nanotips. *Phys. Rev. Lett.* **2007**, *98*, 043907.
19. Biagioni, P.; Celebrano, M.; Savoini, M.; Grancini, G.; Brida, D.; Mátéfi-Tempfli, S.; Mátéfi-Tempfli, M.; Duò, L.; Hecht, B.; Cerullo, G.; Finazzi, M. Dependence of the Two-Photon Photoluminescence Yield of Gold Nanostructures on the Laser Pulse Duration. *Phys. Rev. B* **2009**, *80*, 045411.
20. Biagioni, P.; Brida, D.; Huang, J.-S.; Kern, J.; Duò, L.; Hecht, B.; Finazzi, M.; Cerullo, G. Dynamics of Four-Photon Photoluminescence in Gold Nanoantennas. *Nano Lett.* **2012**, *12*, 2941–2947.
21. Imura, K.; Nagahara, T.; Okamoto, H. J. Near-Field Two-Photon-Induced Photoluminescence from Single Gold Nanorods and Imaging of Plasmon Modes. *J. Phys. Chem. B* **2005**, *109*, 13214–13220.
22. Mooradian, A. Photoluminescence of Metals. *Phys. Rev. Lett.* **1969**, *22*, 185–187.
23. Boyd, G. T.; Yu, Z. H.; Shen, Y. R. Photoinduced Luminescence from the Noble Metals and its Enhancement on Roughed Surfaces. *Phys. Rev. B* **1986**, *33*, 7923–7936.
24. Huang, J.-S.; Callegari, V.; Geisler, P.; Brüning, C.; Kern, J.; Prangsma, J. C.; Wu, X.; Feichtner, T.; Ziegler, J.; Weinmann, P.; *et al.* Atomically Flat Single-Crystalline Gold Nanostructures for Plasmonic Nanocircuitry. *Nat. Commun.* **2010**, *1*, 150.
25. Rhada, B.; Arif, M.; Datta, R.; Kundu, T. K.; Kulkarni, G. U. Movable Au Microplates as Fluorescence Enhancing Substrates for Live Cells. *Nano Res.* **2010**, *3*, 738–747.
26. Radha, B.; Kulkarni, G. U. Giant Single Crystalline Au Microplates. *Curr. Sci.* **2012**, *102*, 70–77.
27. Sell, A.; Krauss, G.; Scheu, R.; Huber, R.; Leitenstorfer, A. 8-fs Pulses from a Compact Er:fiber System: Quantitative Modeling and Experimental Implementation. *Opt. Exp.* **2009**, *17*, 1070–1077.
28. Brida, D.; Krauss, G.; Sell, A.; Leitenstorfer, A. Ultrabroadband Er:fiber Lasers. *Laser Photonics Rev.* **2014**, *8*, 409–428.
29. Garcia de Abajo, F. J.; Howie, A. Retarded Field Calculation of Electron Energy Loss in Inhomogeneous Dielectrics. *Phys. Rev. B* **2002**, *65*, 115418.

30. Hohenester, U.; Trügler, A. MNPBEM—A Matlab Toolbox for the Simulation of Plasmonic Nanoparticles. *Comput. Phys. Commun.* **2012**, *183*, 370–381.
31. Johnson, P. B.; Christy, R. W. Optical Constants of the Noble Metals. *Phys. Rev. B* **1972**, *6*, 4370–4380.
32. Malitson, I. H. Interspecimen Comparison of the Refractive Index of Fused Silica. *J. Opt. Soc. Am.* **1965**, *55*, 1205–1208.